International Journal of
*Molecular Sciences*

MDPI

*Article*

# Photoelectric Performance of Two-Dimensional n-$MoS_2$ Nanosheets/p-Heavily Boron-Doped Diamond Heterojunction at High Temperature

**Deyu Shen, Changxing Li, Dandan Sang *, Shunhao Ge, Qinglin Wang and Dao Xiao ***

School of Physics Science and Information Technology, Liaocheng University, Liaocheng 252000, China; 2022406623@stu.lcu.edu.cn (D.S.); 17853058528@163.com (C.L.); gsh113026@163.com (S.G.); wangqinglin@lcu.edu.cn (Q.W.)
* Correspondence: sangdandan@lcu.edu.cn (D.S.); 15853137007@163.com (D.X.)

**Abstract:** Two-dimensional (2D) n-$MoS_2$ nanosheets (NSs) synthesized via the sol–gel method were deposited onto p-type heavily boron-doped diamond (BDD) film to form a n-$MoS_2$/p-degenerated BDD (DBDD) heterojunction device. The PL emission results for the heterojunction suggest strong potential for applications using yellow-light-emitting optoelectronic devices. From room temperature (RT) to 180 °C, the heterojunction exhibits typical rectification characteristics with good results for thermal stability, rectification ratio, forward current decrease, and reverse current increase. Compared with the n-$MoS_2$/p-lightly B-doped (non-degenerate) diamond heterojunction, the heterojunction demonstrates a significant improvement in both its rectification ratio and ideal factor. At 100 °C, the rectification ratio reaches the maximum value and is considered an ideal high temperature for achieving optimal heterojunction performance. When the temperature exceeds 140 °C, the heterojunction transforms into the Zener diode. The heterojunction's electrical temperature dependence is due to the Fermi level shifting resulting in the weakening of the carrier interband tunneling injection. The n-$MoS_2$ NSs/p-DBDD heterojunction will broaden future research application prospects in the field of high-temperature consumption in future optoelectronic devices.

**Keywords:** n-$MoS_2$ NSs/p-DBDD heterojunction; photoluminescence; high temperature; electrical transport behavior



Academic Editor: Dongho Kim

Received: 1 April 2025
Revised: 29 April 2025
Accepted: 7 May 2025
Published: 9 May 2025

**Citation:** Shen, D.; Li, C.; Sang, D.; Ge, S.; Wang, Q.; Xiao, D. Photoelectric Performance of Two-Dimensional n-$MoS_2$ Nanosheets/p-Heavily Boron-Doped Diamond Heterojunction at High Temperature. *Int. J. Mol. Sci.* **2025**, *26*, 4551. https://doi.org/10.3390/ijms26104551



## 1. Introduction

The transition metal disulfide structure $MoS_2$ is one of the typical channel materials used for the semiconductor p–n junction due to its atomically thin n-type properties [1]. It can be referred to as single-layer or multi-layer, corresponding to its number of layers, and the external electric field can be adjusted from the direct band gap semiconductor (1.9 eV) to the natural indirect band gap (1.2 eV), allowing the tunable and large-scale applications of its electronic and optoelectronic properties [2]. With the increasing demand for nano-materials in optoelectronic devices, nanosized $MoS_2$ appears to solve various problems encountered in developing excellent optoelectronic devices [3,4], such as transistors [5], sensors [6], LEDs [7], and photodetectors [8,9], because of its good mechanical properties, high carrier mobility, high absorption coefficient and strong electron hole constraints. $MoS_2$ has become a top choice to replace previous materials as we enter the new development stage of the nano-era [10]. However, heterostructures formed through different morphologies of $MoS_2$ nanostructures (such as 2D thin films and nanosheets),

which have been combined with various substrates including $MoSe_2$ [11], $WSe_2$ [12,13], GaN [14], GaAsSb [15], $BA_2PbBr_4$ [16] and $MoGe_2N_4$ [17] in recent decades, are mostly confined to room-temperature practical applications. Working in the harsh environments of the heterojunction (high temperature, strong radiation, and high pressure), they still face challenges such as device failure and unsatisfactory performance [18]. Boron-doped diamond (BDD) is usually designed and applied in new high-quality high-temperature resistant optoelectronic devices due to its wide band gap, strong chemical stability, and high thermal conductivity in a p-type semiconductor [19]. At present, typical n-type nanostructured semiconductors (such as ZnO [20], $Ga_2O_3$ [21], and $WO_3$ [22]) have been used to form p–n heterojunction devices with p-type diamond to construct high-quality new diode terminal extension devices. Recently, we investigated the optoelectrical carrier transport behavior of an n-$MoS_2$/p-light B-doped (non-degenerate) diamond heterojunction, which has typical rectification characteristics when working in high-temperature environments [23]. Nevertheless, p-diamond has degenerative characteristics and likely generates band-to-band tunneling through heavily doping boron elements, causing its valence band to lie below the Fermi level [24]. This significantly affects the electrical properties of heterojunctions when combined with other n-type semiconductors [25,26]. Considering the possibility of carrier transport behavior change caused by a heterojunction composed of n-$MoS_2$ and p-DBDD, in this innovative research study, a 2D n-$MoS_2$ NSs/p-DBDD film heterojunction was designed, and the optoelectrical carrier transport performance was analyzed in depth. Compared with $MoS_2$/Si devices [26] and type-II p-$MoS_2$/n-InSe vdWs heterojunctions [27,28], the n-$MoS_2$ NSs/p-DBDD heterojunction demonstrates superior performance in both its maximum rectification ratio and turn-on voltage, while also exhibiting enhanced high-temperature stability [29]. From room temperature (25 °C, RT) to 180 °C, the heterojunction demonstrates representative rectification properties with excellent thermal stability. The rectification ratio and forward current decrease, and the reverse current increases. The rectification ratio reaches its maximum at 100 °C. Compared with the n-$MoS_2$/p-lightly B-doped (non-degenerate) diamond heterojunction in our previous work, this heterojunction demonstrates a significant improvement in both its rectification ratio and ideality factor. The fabricated n-$MoS_2$ NSs/p-DBDD heterojunction demonstrates superior current density and evolves into a Zener diode with increasing temperature, while the n-$MoS_2$ NSs/p-lightly BDD heterojunction transitions into the reverse diode with increasing temperature. The optoelectrical transport behavior depending on temperature was analyzed through a combined energy band diagram and semiconductor theoretical model, which provides a new direction for high-quality research and development in n-$MoS_2$ NSs-related heterojunction optoelectronic devices in harsh environments.

## 2. Results and Discussion

Figure 1a–c displays the morphological characteristics of the 2D n-$MoS_2$ NSs with a size range of 1 to 3 μm. Compared to the p-light B-doped diamond film without twinning and with smoother crystallographic facets described in our previous work, the p-degenerated B-doped diamond films exhibit obvious twinned crystal characteristics. The twinned crystal and abundant grain boundaries of p-degenerated BDD films are beneficial in the nucleation of $MoS_2$ NSs. The $MoS_2$ NSs are densely and randomly distributed on p-DBDD film with a lateral size of about 1.1 μm and a thickness of 98.4 nm. The thickness of 96 nm obtained by local scanning with an atomic force microscope (AFM) confirmed the accuracy of the SEM results shown in Figure 1d,e. The 2D $MoS_2$ NSs fixed on p-DBDD film show a uniform coverage and a large leakage boundary and specific surface area, indicating outstanding photoelectric detection advantages [30]. The element-mapping measurement of the $MoS_2$ NSs was further confirmed according to the EDS mapping of the

spectral area, as shown in Figure 1f. Our observations showed that the elements detected at the heterojunction are C, Mo, and S, as shown in Figure 1g–i which proves that the elements C, Mo, and S coexist and have a high purity. The above characterization proved the successful synthesis of the 2D $MoS_2$ NSs on p-DBDD substrates, and no other peaks related to impurities were detected [31].

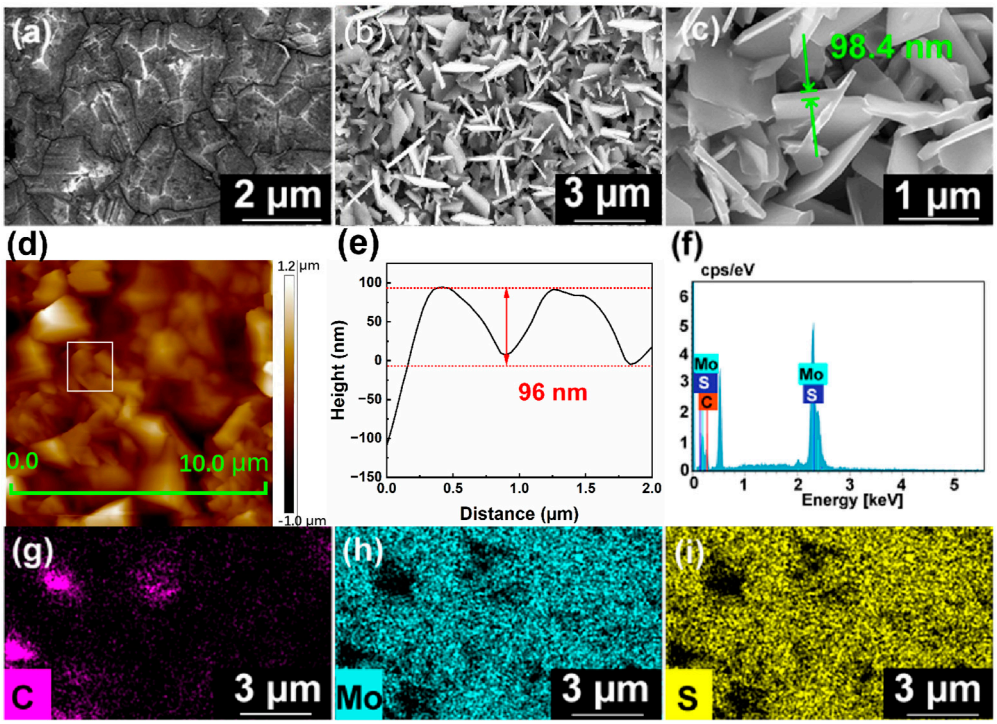


**Figure 1.** SEM of (**a**) the p-DBDD film. (**b**,**c**) the $MoS_2$ NSs. (**d**) AFM image of $MoS_2$ NSs on p-DBDD film. (**e**) The cross-section of AFM. (**f**) EDS spectra of n-$MoS_2$ NSs/p-DBDD heterojunction. (**g**–**i**) EDS mapping images of C, Mo, and S.

Figure 2a shows the XRD image of the n-$MoS_2$ NSs/p-DBDD heterojunction. In addition to the diffraction peaks of (111) and (220) diamond films at 43.82° and 75.24°, three comparatively sharp diffraction peaks were observed at 14.37°, 61.58° and 68.99°, respectively, which can be attributed to (002), (107), and (201) of 2H-$MoS_2$ (JCPD 37-1492). The diffraction peaks at 33.51° and 55.97° are attributed to the presence of (101) and (106) crystal faces in the $MoS_2$ structure [32]. The (220) peak of the diamond film is slightly larger than the (111) peak, indicating that the growth rate of the (220) crystal plane of diamond is greater than that of the (111) plane. Li et al. [33] mentioned in their study that the concentration of the B element is closely related to the preferred orientation of diamond during the CVD growth stage. The intensity ratio of (111) and (220) first decreases and then increases with the increase in B concentration, which is consistent with our experimental results. Figure 2b displays the typical Raman image of the n-$MoS_2$ NSs/p-DBDD heterojunction. The peak in diamond film at 1330 $cm^{-1}$ comes from the central phonon band, and there is a wider Raman peak at 1520 $cm^{-1}$, meaning that there is a graphite phase in addition to the diamond phase [34]. In order to obtain accurate information about the graphite phase, we fitted the data in the illustration with Lorentz. The Raman peak at 1330 $cm^{-1}$ is in the D-band. Generally, the D-band is more obvious in low-doped diamond films [35]. The Raman peak at 1520 $cm^{-1}$ is in the G-band, which is attributed to the bond stretching of the $sp^2$ hybrid orbital of heavily boron-doped diamond [36]. The two peaks at 289 and 376 $cm^{-1}$ match the $E_{1g}$ and $E^1{}_{2g}$ Raman vibration modes of the 2D n-$MoS_2$ NSs [37]. These demonstrate the presence of a 2H-$MoS_2$ phase

with semiconductor characteristics [38]. In addition, the J1 (154 $cm^{-1}$) band specifies the in-plane shear pattern of one side of the alternating chain relative to the other side [39]. The vibration mode of J2 (241 $cm^{-1}$) is connected with the displacement of the S atomic layer and Mo atoms, while the J3 mode obtained at 336 $cm^{-1}$ includes the stretching of one side of the serrated chain with respect to the other side [40]. All vibration J modes are ascribed to the twisted 1T phase superlattice structure. Therefore, the n-$MoS_2$ NSs can reveal both metallic and semiconductor features (2H-$MoS_2$ phase) simultaneously.

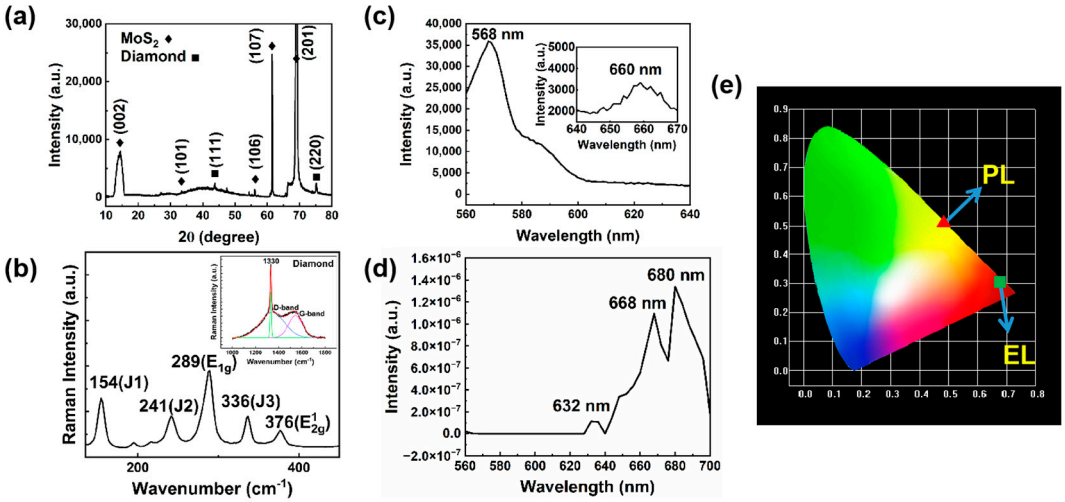


**Figure 2.** (**a**) XRD pattern (**b**) Raman pattern of n-$MoS_2$ NSs/p-DBDD heterojunction; the inset displays the Raman detection of p-DBDD. (**c**) PL spectra of n-$MoS_2$ NSs/p-DBDD heterojunction. (**d**) EL spectra of n-$MoS_2$ NSs/p-DBDD heterojunction. (**e**) CIE chromaticity diagram for PL and EL.

Figure 2c shows the photoluminescence (PL) spectra excited at 532 nm in the n-$MoS_2$ NSs/p-DBDD heterojunction. There is an obvious peak at 568 nm (2.18 eV) due to the transition of exciton A [41,42]. The characteristic broad peak at 660 nm (1.87 eV) is caused by the recombination of the A exciton [43]. In order to further verify the emission color quality of the device, the PL emission CIE color coordinates as shown in Figure 2e, are calculated, and the chromaticity coordinates appear around (0.492, 0.505), which indicates that the n-$MoS_2$ NSs/p-DBDD heterojunction shows promise for applications in the research and development of yellow-light-emitting optoelectronic devices. In addition, the electroluminescence (EL) of the device, as observed in Figure 2d, has rich spectral characteristics. In 2D $MoS_2$, excitons dominate the absorption and emission characteristics and the recombination process directly related to bound excitons is determined from the angle of EL. $MoS_2$ has application value as a tunable portable optical transmitter in which EL is usually confined to the area adjacent to the electrical contact and depends on the hot carrier process [44]. The EL spectrum of the device has three obvious luminescence peaks in the red region. The EL emission peaks at 668 nm and 680 nm are allocated to exciton emission in $MoS_2$ [45,46], while the emission peaks at 632 nm are allocated to exciton B emission. As shown in Figure 2e, CIE color coordinates of EL emission data appear near the red emission region (0.309, 0.694). Compared with the n-$MoS_2$ NSs/p-non-degenerated BDD heterojunction described in our previous work, the intensity of photoluminescence and electroluminescence is doubled, the PL emission changes from light blue to light yellow, and the EL emission changes from green to red [23].

In order to avoid the short-circuiting of the electrodes, the conductive surface of ITO was used as a conductive cathode in contact with the surface of n-$MoS_2$ NSs, and the p-DBDD film was used as a conductive anode with the cathode and anode separated by insulating adhesive. Silver paste and wires were pasted to the conductive side of

the ITO conductive glass as the negative electrode. We fixed the p-DBDD film as the positive electrode and the conductive side of the ITOs so that they were in contact with the $MoS_2$ nanosheets, to form a pathway. The size of the prepared heterojunction device is 0.25 × 0.25 cm, as shown in Figure 3a. The *I-V* characteristics of the Ag contacts to DBDD and the ITO curve show linear properties indicating an ohmic contact (Figure 3b). The Hall test shows that the p-DBDD has a carrier concentration of $5.8 \times 10^{21}$, a resistivity of $1.05 \times 10^{-3}$, and a mobility of 6.8 $cm^2\ V^{-1}\ s^{-1}$. Figure 3a–f suggest the electrical properties of the n-$MoS_2$ NSs/p-DBDD heterojunction gauged from RT to 180 °C. The *I-V* curve shows good rectification performance for all temperatures. The turn-on voltages are about 0.2 V at RT, 0.7 V at 100 °C, 0.3 V at 120 °C, 1 V at 140 °C, 2.1 V at 160 °C, and 0.7 V at 180 °C. With the temperature increasing, the forward current decreases as the bias increases. At RT, the rectification ratio is about 34.46, and the forward current is 0.16 A at 6 V, which is 34 times higher than the n-$MoS_2$ NSs/p-non-degenerated BDD heterojunction reported in our previous work [23]. When the temperature rises to 100 °C, the *I-V* characteristic shows fantastic rectification performance, achieving a rectification ratio of $8.11 \times 10^6$ and a decrease in the reverse saturation current of $5.18 \times 10^{-9}$ A. Thus, 100 °C is believed to be the optimal temperature, with excellent performance, for forward rectifier diode n-$MoS_2$ NSs/p-DBDD heterojunction. A Zener diode was observed when the temperature reached 140–180 °C. When the breakdown voltage is lower than $4E_g/q$, the reverse breakdown can be ascribed to the Zener tunneling effect, where $E_g$ and $q$ are the semiconductor bandgap and electronic charge, respectively. This device has good application potential for analog circuits and small signal detectors [47]. A noteworthy detail is that the reverse current of the n-$MoS_2$ NSs/p-DBDD heterojunction begins to be larger than that at 160 °C and 180 °C, where the rectification ratio is 0.459 and 0.671, and the reverse conduction voltage is 2.1 and 0.7 V, respectively, as shown in Table 1. This is attributed to the increase in reverse carrier tunneling at heterojunctions at high temperatures, while the n-$MoS_2$ NSs/p-non-degenerated BDD heterojunction reported in this paper transforms into a reverse diode with increasing temperatures. In addition, the rectification ratio shows a trend of first increasing, then decreasing, and finally increasing again. Due to the thermal excitation effect, the rectification ratio reaches its maximum value of $8.11 \times 10^6$ at 100 °C. At 160 °C, due to the enhancement of reverse tunneling, the rectification ratio drops to the minimum value of 0.459. Compared with the n-$MoS_2$ NSs/p-non-degraded BDD heterojunction, the n-$MoS_2$ NSs/p-DBDD heterojunction has a better rectification ratio at room temperature and high temperatures. At 100 °C, the rectification ratio of n-$MoS_2$ NSs/p-DBDD increased by $7.64 \times 10^6$ times, which may be due to the addition of B atoms and the high concentration of p-degenerate diamond carriers in heavily doped diamond, resulting in increased carrier injection and tunneling [23].

In order to further explore the electrical transmission behavior at the n-$MoS_2$ NSs/p-DBDD heterojunction, Figure 3h,i is combined with the ideal diode in Equations (1) and (2) [48,49]:

$$I = I_s[\exp(\frac{qV}{nkT}) - 1], \quad (1)$$

with

$$I_s = AA^* \cdot \exp\left(\frac{-q\Phi_B}{kT}\right), \quad (2)$$

where $I_s$ is the reverse saturation current, $q$ is the electronic charge, $V$ is the applied voltage, $n$ is the ideal coefficient, $k$ is the Boltzmann constant, $T$ is the absolute temperature, $A$ is the contact area, and $A^*$ is the effective Richardson constant. On the basis of the 0.1–0.5 V region, the ideality factor ($n$ values) of the n-$MoS_2$/p-DBDD is 8.98–9.33 from RT to 180 °C, which indicates that the positive values of n-$MoS_2$ NSs/p-DBDD are stable. The $n$ value is

greater than 2, demonstrating that the n-$MoS_2$/p-DBDD heterojunction displays nonideal thermal emission properties, which may be due to the inhomogeneity in barrier height, non-uniform interface thickness, and non-uniform atom distribution at the n-$MoS_2$ NSs/p-DBDD interface [50,51]. It can be noted that the result for the $n$ value is significantly lower than that of the reported n-$MoS_2$/p-lightly boron doped BDD heterojunction (8.6–10.2) [52].

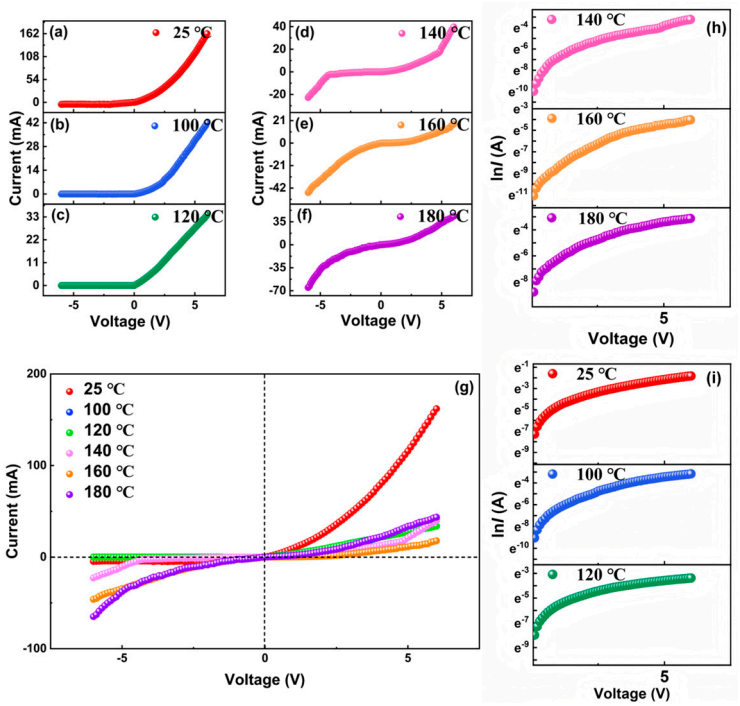


**Figure 3.** (**a**–**g**) *I-V* plots of n-$MoS_2$ NSs/p-DBDD heterojunction at RT, 100 °C, 120 °C, 140 °C, 160 °C, and 180 °C. The inset in (**a**) shows the schematic diagram of the n-$MoS_2$ NSs/p-DBDD heterojunction device. The inset in (**b**) shows the Ag/BDD/Ag and Ag/ITO/Ag ohmic contact. (**h**,**i**) ln*I-V* curves.

**Table 1.** I-V behavior of device at various temperatures.

| Temperature (°C) | RT | 100 °C | 120 °C | 140 °C | 160 °C | 180 °C |
|---|---|---|---|---|---|---|
| Current at 6 V (A) | 0.167 | 0.042 | 0.033 | 0.039 | 0.017 | 0.043 |
| Current at −6 V (A) | 0.004 | $5.18 \times 10^{-9}$ | $3.78 \times 10^{-7}$ | 0.022 | 0.046 | 0.064 |
| Rectification ratio | 41.75 | $8.11 \times 10^{6}$ | $8.73 \times 10^{4}$ | 1.772 | 0.459 | 0.671 |
| Turn on voltage (V) | 0.2 | 0.7 | 0.3 | 1 | 2.1 | 0.7 |
| Ideality factor | 8.98 | 8.82 | 9.73 | 7.78 | 9.71 | 9.33 |

Based on the phenomenon of temperature-induced changes in the current and rectification ratio, the equilibrium energy band diagram for n-$MoS_2$ NSs/p-DBDD was established, using the Anderson model to explain the carrier migration and barrier variation behavior. Reasonable calculation shows that the conduction band (CB) offset $\Delta E_C$ (3.8 eV) is 10 times higher than the valence band (VB) offset $\Delta E_V$ (0.37 eV), meaning that the injection current is primarily involved in the injected holes in VB. Due to the small VB barrier height at RT, the carrier tunneling from the VB to the defect level band stemming from the $MoS_2$ NSs surface state is occupied and exhibits a relatively higher current. Compared with p-non-degenerated BDD, the $E_F$ may approach the band edge and enter into the VB of diamond. The carriers can tunnel from the VB of diamond to the CB of $MoS_2$ when forward bias is exerted and show a reduced valence band barrier, higher forward current, and lower diode conduction voltage (Figure 4a,b). In contrast with p-non-degenerated BDD, the Fermi level of which resides within the forbidden band (exhibiting a diffusion-dominated current), the

Fermi level of the p-DBDD resides within the valence band (exhibiting tunneling-dominated current) at room temperature. Thus, this shows a relatively high current performance compared to the p-non-degenerated BDD in our previous work. At the high temperature of 120 °C, the barrier height of the VB offset increases, which makes it difficult for carriers to transition from VB to the defect energy band, and the tunneling current gradually disappears. At this time, it is transformed into an ordinary p–n junction diode and shows a low forward current and turn-on voltage (Figure 4c). At 180 °C (Figure 4d), the p-DBDD and n-$MoS_2$ thermally activate more charge carriers. In addition, due to the presence of a large number of free surface states and a larger surface-area-to-volume ratio in $MoS_2$ NSs, n-$MoS_2$ NSs form near-degenerate semiconductors that primarily determine electrical properties [53,54]. The $E_F$ may enter the valence band of n-$MoS_2$ and the conduction band of p-DBDD near the edge of the band. This induces an increased valence band barrier height. When a bias is applied, as the tunneling current increases, carriers possibly tunnel from the valence band of n-$MoS_2$ to the conduction band of p-DBDD with the type of Zener diode (Figure 3f).

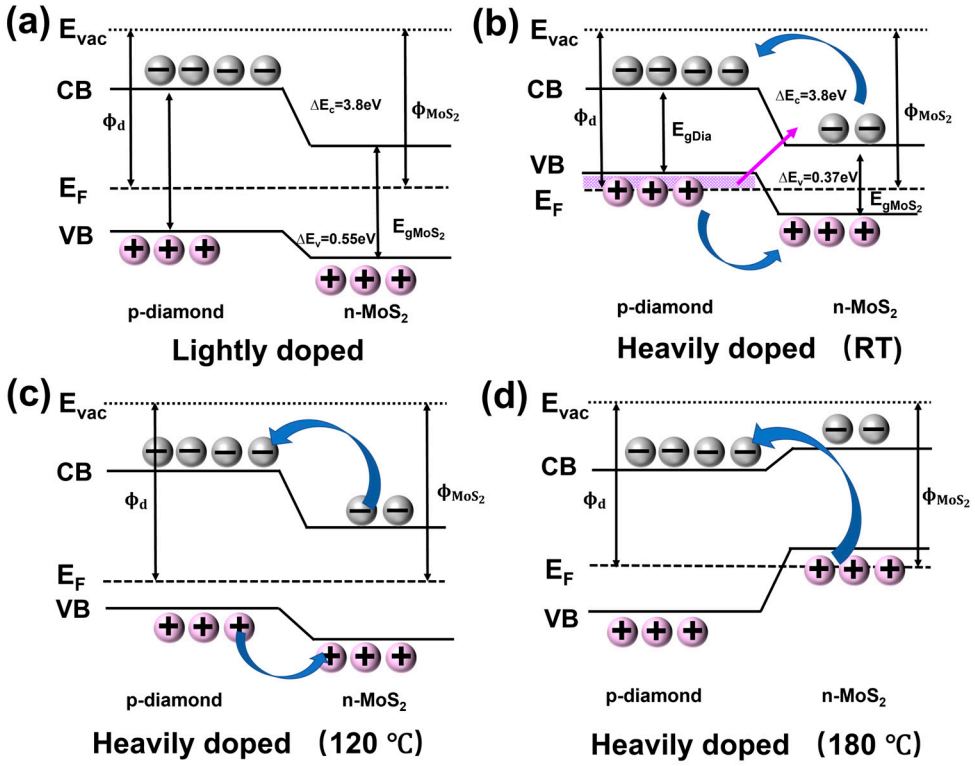


**Figure 4.** Energy band diagrams of (**a**) n-$MoS_2$ NSs/p-non-degenerated BDD heterojunction at RT; n-$MoS_2$ NSs/p-DBDD heterojunction at (**b**) RT, (**c**) 120 °C, (**d**) 180 °C.

The tunneling probability can be expressed using the following simplified relationship:

$$T_B = \exp(-2 \times \frac{\sqrt{2m\Delta V}}{\hbar} \times w_B) \quad (3)$$

where $T_B$ represents the tunneling probability, $\Delta V$ denotes the barrier height, and $w_B$ corresponds to the barrier width. This relationship indicates an inverse proportionality between the tunneling probability and both barrier dimensions: higher barriers (increased $\Delta V$) and wider barriers (larger $W_B$) result in a reduced tunneling probability. When the temperature rises, the n-$MoS_2$/p-DBDD heterojunction exhibits a decreased barrier height and narrowed barrier width, leading to enhanced tunneling probability and consequently

an increased tunneling current. The experimental current-voltage characteristics provide direct evidence supporting this theoretical framework [55].

The carrier migration behavior can also be explained via the variation of work function, as calibrated in Figure 4. The work function was computed using the following equation:

$$\phi = E_{vac} - E_F \quad (4)$$

where $E_{vac}$ is the energy of the vacuum level [56]. Work function values are indicative of the thermodynamic stability of electrons in the respective components of heterostructures, due to which, upon making contact in the heterostructures, the migration of electrons occurs, due to the electron chemical potential difference at the interface, until reaching fermi-level equilibration. The difference in the work function of the heterojunction with the change in temperature leads to the rearrangement of the electron density at the heterojunction cross-section and generates an induced electric field, which promotes the separation and transfer of electrons and holes. With the increase in temperature, the work function of heterojunction p-diamond decreases, and the work function of n-$MoS_2$ increases, meaning that the interface barrier of the heterojunction decreases and more carrier injection is generated at high temperatures, leading to an increase in the tunneling current [57].

The curves at all temperatures in Figure 5a,b are divided into three regions to explore the current transfer mechanism. For low forward voltages (region I), the electrical properties at 25 °C, 100 °C, 120 °C, 140 °C, 160 °C, and 180 °C are directly correlated with the temperature and comply with the power laws of $I$-$V^{1.18}$, $I$-$V^{1.22}$, $I$-$V^{1.06}$, $I$-$V^{1.45}$, $I$-$V^{1.14}$, and $I$-$V^{1.09}$, respectively. The $I$-$V$ characteristics of the n-$MoS_2$ NSs/p-DBDD heterojunction follow the ohmic laws with a linear relationship at a low voltage at all temperatures [58]. In region II, the heterojunction generally shows the $I$-exp($V$) relationship attributed to the existence of a composite tunneling performance due to the wide bandgap semiconductors of $MoS_2$ and diamond material. By fitting the curve of region II, the injection efficiency constant values were calculated to be 0.63, 0.86, 0.56, 0.67, 1.32, and 0.74 at 25 °C, 100 °C, 120 °C, 140 °C, 160 °C, and 180 °C, respectively [59]. At 160 °C, the exponent value was closest to the standard vacuum diode value (1.5). At the higher voltage region III, the current transport properties comply with the laws of $I$-$V^{1.81}$, $I$-$V^{1.72}$, $I$-$V^{1.14}$, $I$-$V^{3.61}$, $I$-$V^{2.21}$, and $I$-$V^{1.75}$ of 25 °C, 100 °C, 120 °C, 140 °C, 160 °C, and 180 °C, respectively. Current has an exponential relationship with voltage, and the exponents are greater than 2, which is normally attributed to the conduction model of space charge limiting current (SCLC) transmission model, which indicates that the SCLC mechanism is limited by a single dominant trap level [60]. The SCLC model with restricted traps can account for exponential values close to 2. At high temperatures, the number of excited holes increases, accumulating and expanding the space charge region within the junction, and, according to the SCLC model, the current mechanism changes from $J \propto V^2$ to $J \propto V^{3/2}$, and thus the exponent is raised to a value greater than 2. At the higher temperature of 180 °C, the exponent falls down again, exhibiting an almost-linear relationship, close to the ohmic–voltage–current relationship, because fewer holes can be excited for injection from diamond VB to $MoS_2$ VB due to the higher energy levels, and this mainly occurs through the tunneling effect [61].

The interface carrier transmission performance at the n-$MoS_2$ NSs/p-DBDD heterojunction can be investigated by fitting the plots of $\ln(I/V^2)$ versus $1/V$ into three situations (Figure 5c,d). (I) For low bias voltage at high temperatures, multiple carriers pass through the interface with the energy produced by thermal excitation to overcome the interface barrier. The carriers transport mechanism can be illustrated using Equation (5) to interpret thermionic emission:

$$\mathrm{I} = AA^{*} \exp\left[\frac{-\left(\varnothing_b - \sqrt{\frac{q^3 V}{4\pi\varepsilon_0\varepsilon_r d}}\right)}{KT}\right], \quad (5)$$

where $A$ is the area of the heterojunction, $A^*$ is the Richardson constant, $d$ is the height of the potential barrier at the interface, $\varnothing_b$ is the height of the potential barrier at $T = 0$ K, $\varepsilon_0$ is the dielectric constant of the vacuum, and $\varepsilon_r$ is the dielectric constant of the semiconductor. Thus, the capability of thermionic emission to conquer the interface barrier height is dependent on the demand excitation temperature. As the temperature is insufficient to allow carriers to pass through the interface barrier, the carrier transfer is primarily concerned with the interface barrier tunneling mechanism, which is identical to the energy band diagram illustration. (II) The interfacial carrier transfer mechanism for low bias voltage can be expounded by coupling the direct tunneling and energy band diagram (Equation (6)):

$$\ln\left(\frac{I}{V^2}\right) \propto \ln\left(\frac{1}{V}\right) - \frac{4\pi d\sqrt{2m\varnothing_b}}{h}, \quad (6)$$

where $h$ is Planck's constant, and $m$ is the charge carrier effective mass. (III) For the higher voltage, the carrier transport mechanism primarily involves Fowler–Nordheim (F–N) tunneling and is shown in Equation (7):

$$\ln\left(\frac{1}{V^2}\right) \propto -\frac{1}{V}\left(\frac{8\pi d\sqrt{2m\varnothing_b^3}}{h}\right), \quad (7)$$

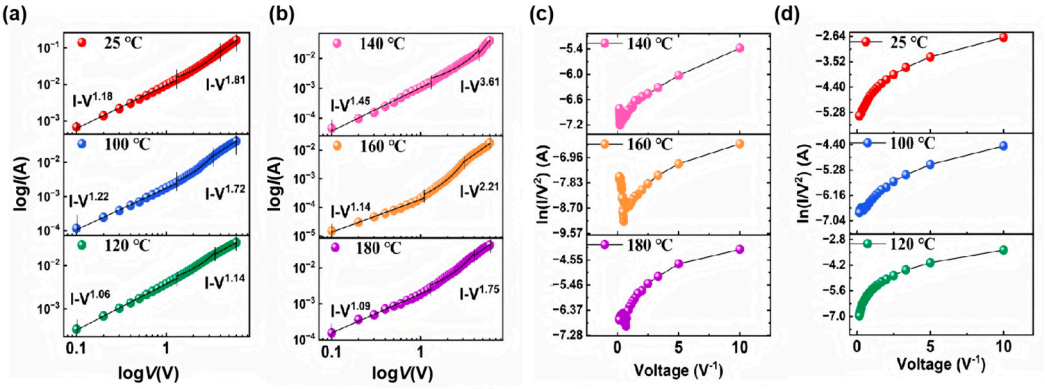


**Figure 5.** (**a**,**b**) log$I$-log$V$ plots; (**c**,**d**) ln($I/V^2$) versus $1/V$ plots for n-$MoS_2$ NSs/p-DBDD heterojunction from RT to 180 °C.

Therefore, multiple carriers can acquire enough energy to pass through the thermionic emission barrier at high temperatures. Based on bias voltage, the carrier injection could take place in direct tunneling to F–N tunneling at lower temperatures. In addition, the emergence of the inflection point ($V_t$) at RT–140 °C indirectly illustrates the presence of F–N and direct tunneling. As $V_{tRT} > 6.25$ V, $V_{t100} > 2.3$ V, $V_{t100} > 2.3$ V, $V_{t140} > 4.6$ V, $V_{t160} > 2$ V and $V_{t180} > 1.40$ V, 1/V exhibits a negative slope trend, implying that the emergence of the F–N tunneling effect on the carrier electrical transport behavior varied, and 1/V took a logarithmic form, signifying the appearance of a direct tunneling effect. With the F–N tunneling mechanism governing carrier transport, the n-$MoS_2$ NSs/p-non-degenerated BDD heterojunction exhibits a higher turn-on voltage ($V_{tRT} = 7.69$ V, $V_{t100} = 6.67$ V, $V_{t120} = 3.84$ V, and $V_{t140} = 5.56$ V), whereas the n-$MoS_2$ NSs/p-DBDD heterojunction demonstrates significantly reduced thresholds ($V_{tRT} = 6.25$ V, $V_{t100} = 2.3$ V, $V_{t140} = 4.6$ V, $V_{t160} = 2$ V and $V_{t180} = 1.40$ V). Furthermore, compared with the $MoS_2$ NSs/p-non-degenerated BDD heterojunction, the n-$MoS_2$ NSs/p-DBDD heterojunction requires a smaller inflection point voltage and depends more on the F–N tunneling conduction mechanism. The lower inflection point voltage at 160 °C and 180 °C means that the heterojunction is more dependent on the F–N tunneling mechanism, which offers a new perspective on erasing electrons in

the field of memory devices. In addition, the phenomenon of a large reverse current occurring when a large voltage is applied at high temperatures can be attributed to thermionic activated carriers and an amplified tunneling current [62,63].

## 3. Materials and Methods

In an instrument filled with flowing $H_2$ and $CH_4$ gases, heavily boron-doped p-type diamond films were prepared on a silicon wafer substrate by the hot-filament chemical vapor deposition (HFCVD) method. The boron source was provided by liquid trimethyl borate ($(CH_3O)_3B$), which was introduced into the chamber through $H_2$, and the DBDD membrane was obtained by controlling the flow rate of $H_2$. Subsequently, the DBDD membrane was washed with ethanol and then deionized water to remove residual impurities from the surface. The DBDD was not treated with irradiation, acid-boiled, or treated with a high temperature, so it had a hydrogen surface terminal.

$MoS_2$ nanosheets were prepared on DBDD film via the sol–gel method. As shown in Scheme 1, $[(NH_4)_6Mo_7O_{24} \cdot 4H_2O]$ was used as the Mo source, $CH_3CSNH_2$ as the S source, and $C_{14}H_{23}N_3O_{10}$ as the chelating agent. The mixture was stirred continuously for one hour using a magnetic stirrer and dissolved in 8 mL of deionized water to obtain a sol. We placed the DBDD film based on silicon at the center of the spin-coating machine, used a pipette to drop the sol onto the center of the DBDD film, and accelerated from 0 to 3000 rpm within 56 s. We removed the film and set it on a heating table at 60 °C to cure the coating on the DBDD film for 5 min, and then we performed the second deposition through an identical procedure to thicken the nanosheet with the annealing process at 400 °C over 4 h to improve the quality of the bonded device. Scheme 2a illustrates the schematic structure of the n-$MoS_2$ NSs/p-DBDD heterojunction. The $MoS_2$ NSs are brought into contact with the conductive side of transparent indium tin oxide (ITO) glass and secured using cyanoacrylate adhesive to prevent direct contact between the conductive copper wires and $TiO_2$. The BDD at the bottom of the contact can easily cause a short circuit, which can be effectively prevented by employing ITO as a dielectric. The ITO and conductive copper wires are connected with silver paste, respectively, to fabricate the heterojunction anode and cathode. The linear *I-V* characteristics between the ITO/Ag and BDD/Ag contacts demonstrate the linear relationship of an ohmic contact (Scheme 2b).

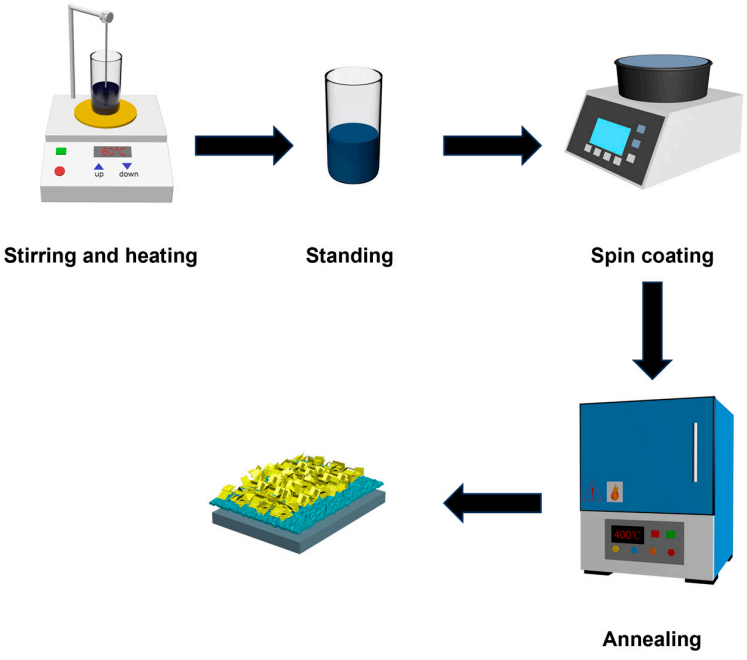


**Scheme 1.** Diagram of synthesis of n-$MoS_2$ NSs/p-DBDD heterojunction via sol–gel method.

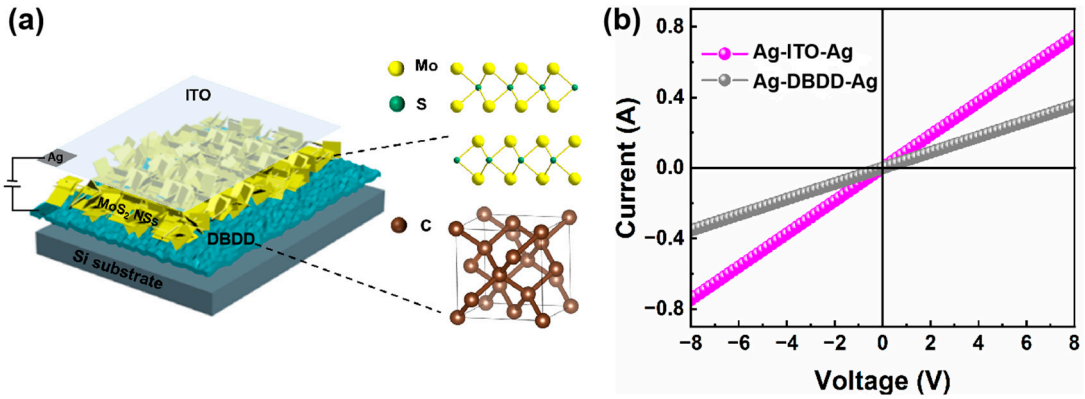


**Scheme 2.** (**a**) The schematic structure of the n-$MoS_2$ NSs/p-DBDD heterojunction. (**b**) The ohmic contact tests for Ag/ITO/Ag and Ag/DBDD/Ag.

A scanning electron microscope with energy dispersive X-ray spectroscopy (SEM, Thermo Fisher Scientific FIB-SEM GX4, produced from Bothell, WA, USA) was used to examine the element distribution and structural morphology of the samples. We set the scanning speed of the X-ray diffractometer (XRD, D8 ADVANCE, produced from Karlsruhe, Germany) at 5°/min to check the phase structure and purity of the sample. The molecular structures of $MoS_2$ NSs and p-degenerated BDD were detected with an excitation wavelength of 532 nm using a Raman spectrometer (Raman, inVia, produced from London, UK), and the heterojunction electrical properties were tested with the Keithley 2400 source (Keithley Instrument, Cleveland, OH, USA). The carrier concentration of the DBDD film was assessed via the Hall effect (ET9110-HS, produced from Beijing, China).

## 4. Conclusions

In conclusion, an n-$MoS_2$ NS/p-DBDD heterojunction was successfully fabricated with obvious twin characteristics and abundant grain boundaries on p-DBDD films, which made the $MoS_2$ NSs easier to nucleate. The *I-V* characteristics of the devices all show rectification characteristics at RT-180 °C, and the rectification ratio reaches the maximum at 100 °C, which is considered the optimal rectification temperature for the heterojunction. In contrast to the n-$MoS_2$ NS/p-lightly BDD heterojunction, which transitions into a reverse diode at elevated temperatures, the fabricated n-$MoS_2$ NS/p-DBDD heterojunction exhibits Zener diode characteristics when operating above 140 °C. A Zener diode was observed when the temperature was above 140 °C. The variation in the electrical transport behavior at different temperatures can mainly be attributed to the shift in the Fermi level and the change in the tunneling current. The rectification ratio and ideal factor of n-$MoS_2$ NS/p-DBDD are significantly superior to those of the prepared n-$MoS_2$ NS/p-non-degenerated BDD heterojunction. A noteworthy detail is that the n-$MoS_2$ NS/p-DBDD heterojunction is more dependent on F–N tunneling and is suitable for operation under high-temperature conditions. The n-$MoS_2$/p-DBDD heterojunction provides an effective reference for applications of memory erasure technology and the development of high-quality devices for use in extreme working environments.

**Author Contributions:** Writing—original draft, D.S. (Deyu Shen) and C.L.; methodology, D.S. (Deyu Shen), C.L., D.S. (Dandan Sang), S.G., D.X. and Q.W.; investigation, D.S. (Deyu Shen), C.L., D.S. (Dandan Sang), S.G., D.X. and Q.W.; conceptualization, D.S. (Deyu Shen), C.L., D.S. (Dandan Sang), D.X. and Q.W.; supervision, D.S. (Dandan Sang), D.X. and Q.W.; writing—review and editing, Q.W. All authors have read and agreed to the published version of the manuscript.

**Funding:** This research was funded by the National Natural Science Foundation of China (Grant Nos. 62104090 and 11604133), the Natural Science Foundation of Shandong Province (ZR2022QF135), the Science and Technology Plan of Youth Innovation Team for Universities of Shandong Province (Grant No. 2019KJJ019), the Introduction and Cultivation Plan of Youth Innovation Talents for Universities of Shandong Province and the Research Funding of Liaocheng University (Grant Nos. 318012016, 318051610, 318052136, and 318051612).

**Data Availability Statement:** Data is contained within the article.

**Conflicts of Interest:** The authors declare that they have no known competing financial interests or personal relationships that could have appeared to influence the work reported in this paper.

## References

1. Liu, L.W.; Liu, C.S.; Huang, X.H.; Zeng, S.F.; Tang, Z.W.; Zhang, D.W.; Zhou, P. Tunable Current Regulative Diode Based on Van der Waals Stacked $MoS_2/WSe_2$ Heterojunction–Channel Field-Effect Transistor. *Adv. Electron. Mater.* **2022**, *8*, 2100869. [CrossRef]
2. Nalwa, H.S. A review of molybdenum disulfide ($MoS_2$) based photodetectors: From ultra-broadband, self-powered to flexible devices. *RSC Adv.* **2020**, *10*, 30529–30602. [CrossRef]
3. Zou, L.R.; Sang, D.D.; Yao, Y.; Wang, X.T.; Zheng, Y.Y.; Wang, N.Z.; Wang, C.; Wang, Q.L. Research progress of optoelectronic devices based on two-dimensional $MoS_2$ materials. *Rare Met.* **2023**, *42*, 17–38. [CrossRef]
4. Zou, L.R.; Lyu, X.D.; Sang, D.D.; Yao, Y.; Ge, S.H.; Wang, X.T.; Zhou, C.D.; Fu, H.L.; Xi, H.Z.; Fan, J.C.; et al. Two-dimensional $MoS_2$/diamond based heterojunctions for excellent optoelectronic devices: Current situation and new perspectives. *Rare Met.* **2023**, *42*, 3201–3211. [CrossRef]
5. Wu, F.; Tian, H.; Shen, Y.; Hou, Z.; Ren, J.; Gou, G.; Sun, Y.; Yang, Y.; Ren, T.L. Vertical $MoS_2$ transistors with sub-1-nm gate lengths. *Nature* **2022**, *603*, 259–264. [CrossRef]
6. Evans, J.M.; Lee, K.S.; Yan, E.X.; Thompson, A.C.; Morla, M.B.; Meier, M.C.; Ifkovits, Z.P.; Carim, A.I.; Lewis, N.S. Demonstration of a Sensitive and Stable Chemical Gas Sensor Based on Covalently Functionalized $MoS_2$. *ACS Mater. Lett.* **2022**, *4*, 1475–1480. [CrossRef]
7. Liu, C.; Lu, Y.; Yu, X.; Shen, R.; Wu, Z.; Yang, Z.; Yan, Y.; Feng, L.; Lin, S. Hot carriers assisted mixed-dimensional graphene/$MoS_2$/p-GaN light emitting diode. *Carbon* **2022**, *197*, 192–199. [CrossRef]
8. Liu, X.; Hu, S.; Lin, Z.; Li, X.; Song, L.; Yu, W.; Wang, Q.; He, W. High-performance $MoS_2$ photodetectors prepared using a patterned gallium nitride substrate. *ACS Appl. Mater. Interfaces* **2021**, *13*, 15820–15826. [CrossRef]
9. Yang, S.; Liu, Y.; Wu, Y.; Guo, F.; Zhang, M.; Zhu, X.; Xua, R.; Hao, L. High-performance flexible photodetectors based on CdTe/$MoS_2$ heterojunction. *Nanoscale* **2024**, *16*, 13932–13937. [CrossRef]
10. Samy, O.; Zeng, S.; Birowosuto, M.D.; El Moutaouakil, A. A review on $MoS_2$ properties, synthesis, sensing applications and challenges. *Crystals* **2021**, *11*, 355. [CrossRef]
11. Jeong, Y.; Lee, H.J.; Park, J.; Lee, S.; Jin, H.J.; Park, S.; Cho, H.; Hong, S.; Kim, T.; Kim, K.; et al. Engineering $MoSe_2/MoS_2$ heterojunction traps in 2D transistors for multilevel memory, multiscale display, and synaptic functions. *Npj 2D Mater. Appl.* **2022**, *6*, 23. [CrossRef]
12. Jeong, M.H.; Ra, H.S.; Lee, S.H.; Kwak, D.H.; Ahn, J.; Yun, W.S.; Lee, J.; Chae, W.S.; Hwang, D.K.; Lee, J.S. Multilayer $WSe_2/MoS_2$ Heterojunction Phototransistors through Periodically Arrayed Nanopore Structures for Bandgap Engineering. *Adv. Mater.* **2022**, *34*, 2108412. [CrossRef] [PubMed]
13. Xiang, X.; Qiu, Z.; Zhang, Y.; Chen, X.; Wu, Z.; Zheng, H.; Zhang, Y. Gain-type photodetector with GFET-coupled $MoS_2/WSe_2$ heterojunction. *J. Alloys Compd.* **2024**, *1002*, 175475. [CrossRef]
14. Jian, P.; Cai, X.; Zhao, Y.; Li, D.; Zhang, Z.; Liu, W.; Xu, D.; Liang, W.; Zhou, X.; Dai, J.; et al. Large-scale synthesis and exciton dynamics of monolayer $MoS_2$ ondifferently doped GaN substrates. *Nanophotonics* **2023**, *12*, 4475–4484. [CrossRef]
15. Wang, W.; Wang, W.; Meng, Y.; Quan, Q.; Lai, Z.; Li, D.; Xie, P.; Yip, S.; Kang, X.; Bu, X.; et al. Mixed-Dimensional Anti-ambipolar Phototransistors Based on 1D GaAsSb/2D $MoS_2$ Heterojunctions. *ACS Nano* **2022**, *16*, 11036–11048. [CrossRef]
16. Parveen, S.; Pal, P.K.; Mukhopadhyay, S.; Majumder, S.; Bisoi, S.; Rahman, A.; Barman, A. Hot carrier dynamics in the $BA_2PbBr_4/MoS_2$ heterostructure. *Nanoscale* **2025**, *17*, 2800. [CrossRef]
17. Nguyena, S.T.; Pham, K.D. Theoretical prediction of the electronic structure, optical properties and contact characteristics of a type-I $MoS_2/MoGe_2N_4$ heterostructure towards optoelectronic devices. *Dalton Trans.* **2024**, *53*, 9072–9080. [CrossRef]
18. Yao, Y.; Sang, D.; Duan, S.; Wang, Q.; Liu, C. Review on the Properties of Boron-Doped Diamond and One-Dimensional-Metal-Oxide Based PN Heterojunction. *Molecules* **2020**, *26*, 71. [CrossRef]
19. Wang, L.; Cheng, S.; Wu, C.; Pei, K.; Song, Y.; Li, H.; Wang, Q.; Sang, D. Fabrication and high temperature electronic behaviors of n-WO3 nanorods/p-diamond heterojunction. *Appl. Phys. Lett.* **2017**, *110*, 052106. [CrossRef]

20. Wang, Q.; Yao, Y.; Sang, X.; Zou, L.; Ge, S.; Wang, X.; Zhang, D.; Wang, Q.; Zhou, H.; Fan, J.; et al. Photoluminescence and Electrical Properties of n-Ce-Doped ZnO Nanoleaf/p-Diamond Heterojunction. *Nanomaterials* **2022**, *12*, 3773. [CrossRef]
21. Lin, W.; Wang, T.T.; Wang, Q.L.; Lv, X.Y.; Li, G.Z.; Li, L.A.; Zou, G.T. Design of vertical diamond Schottky barrier diode with junction terminal extension structure by using the n-$Ga_2O_3$/p-diamond heterojunction. *Chin. Phys. B* **2022**, *31*, 108105. [CrossRef]
22. Yao, Y.; Sang, D.; Duan, S.; Wang, Q.; Liu, C. Excellent optoelectronic applications and electrical transport behavior of the n-$WO_3$ nanostructures/p-diamond heterojunction: A new perspective. *Nanotechnology* **2021**, *32*, 332501. [CrossRef]
23. Zou, L.; Sang, D.; Ge, S.; Yao, Y.; Wang, G.; Wang, X.; Fan, J.; Wang, Q. High-temperature optoelectronic transport behavior of n-$MoS_2$ nanosheets/p-diamond heterojunction. *J. Alloys Compd.* **2024**, *972*, 172819. [CrossRef]
24. Clavel, M.B.; Liu, J.-S.; Meeker, M.A.; Khodaparast, G.A.; Xie, Y.; Heremans, J.J.; Bhattacharya, S.; Hudait, M.K. Electronic and optical properties of highly boron-doped epitaxial Ge/AlAs(001) heterostructures. *J. Appl. Phys.* **2020**, *127*, 075702. [CrossRef]
25. Sang, D.; Liu, J.; Wang, X.; Zhang, D.; Ke, F.; Hu, H.; Wang, W.; Zhang, B.; Li, H.; Liu, B.; et al. Negative differential resistance of n-ZnO nanorods/p-degenerated diamond heterojunction at high temperatures. *Front. Chem.* **2020**, *8*, 531. [CrossRef]
26. Huang, J.; Meng, A.; Zhang, Z.; Ma, G.; Long, Y.; Li, X.; Xiang, B.; Han, P.; He, B. $BiVO_4$/boron-doped diamond heterojunction photoanode with boron doping engineering and enhanced photoelectrocatalytic activity. *Diam. Relat. Mater.* **2023**, *138*, 110226. [CrossRef]
27. Su, T.H.; Chiang, C.H.; Lin, Y.J. Temperature dependence of current–voltage characteristics of $MoS_2$/Si devices prepared by the chemical vapor deposition method. *Microelectron. Reliab.* **2017**, *78*, 374–378. [CrossRef]
28. Li, P.; Yuan, K.; Lin, D.Y.; Wang, T.; Du, W.; Wei, Z.; Watanabe, K. p-$MoS_2$/n-InSe van der Waals heterojunctions and their applications in all-2D optoelectronic devices. *RSC Adv.* **2019**, *9*, 35039–35044. [CrossRef]
29. Zhang, L.; Cheng, S.; Wang, L.; Pei, K.; Li, H. High temperature UV photodetectors based on the negative differential resistance effect of $WO_3$/diamond PN junctions. *Appl. Phys. Lett.* **2023**, *122*, 182102. [CrossRef]
30. Zhang, K.; Feng, S.; Kang, S.; Wu, Y.; Zhang, M.; Wang, Q.; Tao, Z.; Fan, Y.; Lu, W. Hybrid structure of PbS QDs and vertically-few-layer $MoS_2$ nanosheets array for broadband photodetector. *Nanotechnology* **2021**, *32*, 145602. [CrossRef]
31. Zhang, Y.; Zeng, W.; Li, Y. The hydrothermal synthesis of 3D hierarchical porous $MoS_2$ microspheres assembled by nanosheets with excellent gas sensing properties. *J. Alloys Compd.* **2018**, *749*, 355–362. [CrossRef]
32. He, H.Y.; He, Z.; Shen, Q. Efficient hydrogen evolution catalytic activity of graphene/metallic $MoS_2$ nanosheet heterostructures synthesized by a one-step hydrothermal process. *Int. J. Hydrogen Energy* **2018**, *43*, 21835–21843. [CrossRef]
33. Li, H.; Zhang, T.; Li, L.; Lu, X.; Li, B.; Jin, Z.; Zou, J. Investigation on crystalline structure, boron distribution, and residual stresses in freestanding boron-doped CVD diamond films. *J. Cryst. Growth* **2010**, *312*, 1986–1991. [CrossRef]
34. Knight, D.S.; White, W.B. Characterization of diamond films by Raman spectroscopy. *J. Mater. Res.* **1989**, *4*, 385–393. [CrossRef]
35. Kumar, D.; Chandran, M.; Rao, M.S.R. Effect of boron doping on first-order Raman scattering in superconducting boron doped diamond films. *Appl. Phys. Lett.* **2017**, *110*, 191602. [CrossRef]
36. Ferrari, A.C.; Robertson, J. Interpretation of Raman spectra of disordered and amorphous carbon. *Phys. Rev. B* **2000**, *61*, 14095. [CrossRef]
37. Huang, J.; Dong, Z.; Li, Y.; Li, J.; Tang, W.; Yang, H.; Wang, J.; Bao, Y.; Jin, J.; Li, R. $MoS_2$ nanosheet functionalized with Cu nanoparticles and its application for glucose detection. *Mater. Res. Bull.* **2013**, *48*, 4544–4547. [CrossRef]
38. Erkan, S.; Altuntepe, A.; Zan, R. Synthesis of $MoS_2$ thin films using the two-step approach. *Niğde Ömer Halisdemir Üniversitesi Mühendislik Bilim. Derg.* **2023**, *12*, 297–301. [CrossRef]
39. Liu, Z.; Zhao, L.; Liu, Y.; Gao, Z.; Yuan, S.; Li, X.; Li, N.; Miao, S. Vertical nanosheet array of 1T phase $MoS_2$ for efficient and stable hydrogen evolution. *Appl. Catal. B Environ.* **2019**, *246*, 296–302. [CrossRef]
40. Naz, M.; Hallam, T.; Berner, N.C.; McEvoy, N.; Gatensby, R.; McManus, J.B.; Akhter, Z.; Duesberg, G.S. A new 2H-2H′/1T cophase in polycrystalline $MoS_2$ and $MoSe_2$ thin films. *ACS Appl. Mater. Interfaces* **2016**, *8*, 31442–31448. [CrossRef]
41. Yin, W.; Bai, X.; Zhang, X.; Zhang, J.; Gao, X.; Yu, W.W. Multicolor Light-Emitting Diodes with $MoS_2$ Quantum Dots. *Part. Part. Syst. Charact.* **2019**, *36*, 1800362. [CrossRef]
42. Baby, M.; Kumar, K.R. Enhanced luminescence of silver nanoparticles decorated on hydrothermally synthesized exfoliated $MoS_2$ nanosheets. *Emergent Mater.* **2020**, *3*, 203–211. [CrossRef]
43. Ponomarev, E.; Gutiérrez-Lezama, I.; Ubrig, N.; Morpurgo, A.F. Ambipolar light-emitting transistors on chemical vapor deposited monolayer $MoS_2$. *Nano Lett.* **2015**, *15*, 8289–8294. [CrossRef]
44. Ye, Y.; Ye, Z.; Gharghi, M.; Zhu, H.; Zhao, M.; Wang, Y.; Yin, X.; Zhang, X. Exciton-dominant electroluminescence from a diode of monolayer $MoS_2$. *Appl. Phys. Lett.* **2014**, *104*, 193508. [CrossRef]
45. Li, D.; Cheng, R.; Zhou, H.; Wang, C.; Yin, A.; Chen, Y.; Weiss, N.O.; Huang, Y.; Duan, X. Electric-field-induced strong enhancement of electroluminescence in multilayer molybdenum disulfide. *Nat. Commun.* **2015**, *6*, 7509. [CrossRef]
46. Sundaram, R.S.; Engel, M.; Lombardo, A.; Krupke, R.; Ferrari, A.C.; Avouris, P.; Steiner, M. Electroluminescence in single layer $MoS_2$. *Nano Lett.* **2013**, *13*, 1416–1421. [CrossRef]

47. Liu, X.; Qu, D.; Li, H.M.; Moon, I.; Ahmed, F.; Kim, C.; Lee, M.; Choi, Y.; Cho, J.H.; Hone, J.C.; et al. Modulation of quantum tunneling via a vertical two-dimensional black phosphorus and molybdenum disulfide p–n junction. *ACS Nano* **2017**, *11*, 9143–9150. [CrossRef]
48. Di Bartolomeo, A.; Giubileo, F.; Luongo, G.; Iemmo, L.; Martucciello, N.; Niu, G.; Fraschke, M.; Skibitzki, O.; Schroeder, T.; Lupina, G. Tunable Schottky barrier and high responsivity in graphene/Si-nanotip optoelectronic device. *2D Mater* **2016**, *4*, 015024. [CrossRef]
49. Mukherjee, S.; Biswas, S.; Das, S.; Ray, S.K. Solution-processed, hybrid 2D/3D $MoS_2$/Si heterostructures with superior junction characteristics. *Nanotechnology* **2017**, *28*, 135203. [CrossRef]
50. Çetinkaya, H.; Yıldırım, M.; Durmuş, P.; Altındal, Ş. Correlation between barrier height and ideality factor in identically prepared diodes of Al/Bi4Ti3O12/p-Si (MFS) structure with barrier inhomogeneity. *J. Alloys Compd.* **2017**, *721*, 750–756. [CrossRef]
51. Soylu, M.; Yakuphanoglu, F. Analysis of barrier height inhomogeneity in Au/n-GaAs Schottky barrier diodes by Tung model. *J. Alloys Compd.* **2010**, *506*, 418–422. [CrossRef]
52. Kim, J.K.; Cho, K.; Kim, T.Y.; Pak, J.; Jang, J.; Song, Y.; Kim, Y.; Choi, B.Y.; Chung, S.; Hong, W.K.; et al. Trap-mediated electronic transport properties of gate-tunable pentacene/$MoS_2$ pn heterojunction diodes. *Sci. Rep.* **2016**, *6*, 36775. [CrossRef]
53. Kumar, R.; Zheng, W.; Liu, X.; Zhang, J.; Kumar, M. $MoS_2$-Based Nanomaterials for Room-Temperature Gas Sensors. *Adv. Mater. Technol.* **2020**, *5*, 191062. [CrossRef]
54. Rong, P.; Jiang, Y.; Wang, Q.; Gu, M.; Jiang, X.; Yu, Q. Photocatalytic degradation of methylene blue (MB) with $Cu_1$–ZnO single atom catalysts on graphene-coated flexible substrates. *J. Mater. Chem. A* **2022**, *10*, 6231–6241. [CrossRef]
55. Zhong, H.; Quhe, R.; Wang, Y.; Ni, Z.; Ye, M.; Song, Z.; Pan, Y.; Yang, J.; Yang, L.; Lei, M.; et al. Interfacial Properties of Monolayer and Bilayer $MoS_2$ Contacts with Metals: Beyond the Energy Band Calculations. *Sci. Rep.* **2016**, *6*, 21786. [CrossRef]
56. Curry, J.F.; Ohta, T.; DelRio, F.W.; Mantos, P.; Jones, M.R.; Babuska, T.F.; Bobbitt, N.S.; Argibay, N.; Krick, B.A.; Dugger, M.T.; et al. Structurally Driven Environmental Degradation of Friction in $MoS_2$ Films. *Tribol. Lett.* **2021**, *69*, 96. [CrossRef]
57. Singha, S.; Puniaa, R.; Panta, K.K.; Biswasb, P. Effect of work-function and morphology of heterostructure components on $CO_2$ reduction photo-catalytic activity of $MoS_2$-$Cu_2O$ heterostructure. *Chem. Eng. J.* **2022**, *433*, 132709. [CrossRef]
58. Zhang, Y.; Zhuang, Y.; Liu, L.; Qiu, P.; Su, L.; Teng, X.; Fu, G.; Yu, W. The microstructure evolution during $MoS_2$ films growth and its influence on the $MoS_2$ optical-electrical properties in $MoS_2$/p-Si heterojunction solar cells. *Superlattices Microstruct.* **2020**, *137*, 106352. [CrossRef]
59. Dutta, M.; Basak, D. p-ZnO/n-Si heterojunction: Sol-gel fabrication, photoresponse properties, and transport mechanism. *Appl. Phys. Lett.* **2008**, *92*, 212112. [CrossRef]
60. Çaldıran, Z. Modification of Schottky barrier height using an inorganic compound interface layer for various contact metals in the metal/p-Si device structure. *J. Alloys Compd.* **2021**, *865*, 158856. [CrossRef]
61. Yu, Y.; Wang, C.; Jiang, C.; Abrahams, I.; Du, Z.; Zhang, Q.; Sun, J.; Huang, X. Resistive switching behavior in memristors with $TiO_2$ nanorod arrays of different dimensions. *Appl. Surf. Sci.* **2019**, *485*, 222–229. [CrossRef]
62. Padma, R.; Lee, G.; Kang, J.S.; Jun, S.C. Structural, chemical, and electrical parameters of Au/$MoS_2$/n-GaAs metal/2D/3D hybrid heterojunction. *J. Colloid Interface Sci.* **2019**, *550*, 48–56. [CrossRef] [PubMed]
63. Sarker, B.K.; Khondaker, S.I. Thermionic emission and tunneling at carbon nanotube–organic semiconductor interface. *ACS Nano* **2012**, *6*, 4993–4999. [CrossRef] [PubMed]